

# A Multisensor Perspective on the Radiative Impacts of Clouds and Aerosols

DAVID S. HENDERSON

*Department of Atmospheric Science, Colorado State University, Fort Collins, Colorado*

TRISTAN L'ECUYER

*Department of Atmospheric and Oceanic Sciences, University of Wisconsin—Madison, Madison, Wisconsin*

GRAEME STEPHENS

*Jet Propulsion Laboratory, Pasadena, California*

PHIL PARTAIN

*Cooperative Institute for Research in the Atmosphere, Colorado State University, Fort Collins, Colorado*

MIHO SEKIGUCHI

*Tokyo University of Marine Science and Technology, Tokyo, Japan*

(Manuscript received 6 January 2012, in final form 25 October 2012)

## ABSTRACT

The launch of *CloudSat* and *Cloud–Aerosol Lidar and Infrared Pathfinder Satellite Observations (CALIPSO)* in 2006 provided the first opportunity to incorporate information about the vertical distribution of cloud and aerosols directly into global estimates of atmospheric radiative heating. Vertical profiles of radar and lidar backscatter from *CloudSat*'s Cloud Profiling Radar (CPR) and the Cloud–Aerosol Lidar with Orthogonal Polarization (CALIOP) aboard *CALIPSO* naturally complement Moderate Resolution Imaging Spectroradiometer (MODIS) radiance measurements, providing a nearly complete depiction of the cloud and aerosol properties that are essential for deriving high-vertical-resolution profiles of longwave (LW) and shortwave (SW) radiative fluxes and heating rates throughout the atmosphere. This study describes a new approach for combining vertical cloud and aerosol information from *CloudSat* and *CALIPSO* with MODIS data to assess impacts of clouds and aerosols on top-of-atmosphere (TOA) and surface radiative fluxes. The resulting multisensor cloud–aerosol product is used to document seasonal and annual mean distributions of cloud and aerosol forcing globally from June 2006 through April 2011. Direct comparisons with Clouds and the Earth's Radiant Energy System (CERES) TOA fluxes exhibit a close correlation, with improved errors relative to *CloudSat*-only products. Sensitivity studies suggest that remaining uncertainties in SW fluxes are dominated by uncertainties in *CloudSat* liquid water content estimates and that the largest sources of LW flux uncertainty are prescribed surface temperature and lower-tropospheric humidity. Globally and annually averaged net TOA cloud radiative effect is found to be  $-18.1 \text{ W m}^{-2}$ . The global, annual mean aerosol direct radiative effect is found to be  $-1.6 \pm 0.5 \text{ W m}^{-2}$  ( $-2.5 \pm 0.8 \text{ W m}^{-2}$  if only clear skies over the ocean are considered), which, surprisingly, is more consistent with past modeling studies than with observational estimates that were based on passive sensors.

## 1. Introduction

Atmospheric radiative heating is one of the most important factors determining global weather and climate. Clouds and aerosols can exert a strong influence on

regional radiative balance by reflecting shortwave (SW) radiation back to space and emitting longwave (LW) radiation to the surface, providing one of the strongest feedback pathways in the climate system. Knowledge of these competing effects is essential for understanding Earth's climate system, but cloud feedbacks and the magnitude of aerosol forcing remain large unknowns in predicting climate change (Stephens 2005).

---

*Corresponding author address:* David Henderson, Colorado State University, 1371 Campus Delivery, Fort Collins, CO 80523.  
E-mail: henderson@atmos.colostate.edu

Satellites provide an excellent base to measure the energy exchanged among Earth's surface, the atmosphere, and space (VonderHaar and Suomi 1971; Barkstrom 1984; Wielicki et al. 1996; Schiffer and Rossow 1983). The launch of *CloudSat* and *Cloud–Aerosol Lidar and Infrared Pathfinder Satellite Observations (CALIPSO)* (Stephens et al. 2002) in 2006 provided a new opportunity to improve the representation of the vertical distribution of cloud properties in radiative flux calculations. New cloud boundary information from these sensors offers the potential to dramatically reduce errors in cloud boundaries that can reach 1 km or more (e.g., Holz et al. 2008; Menzel et al. 2008; Naud et al. 2005). From the sensitivity studies described below, this improved vertical resolution may reduce errors in global estimates of cloud LW forcing by as much as  $6 \text{ W m}^{-2}$ . The potential for using this new high-vertical-resolution cloud property information to constrain radiative fluxes was demonstrated by L'Ecuyer et al. (2008), who describe a method for inferring LW and SW radiative flux and heating-rate profiles from primarily *CloudSat* observations. The resulting level-2 "Fluxes and Heating Rates" product (2B-FLXHR, release 04) uses vertical distributions of liquid and ice cloud effective radii and water contents from the level-2 cloud water content product (2B-CWC) (Austin 2007; Austin et al. 2009), ancillary temperature and humidity profiles from the European Centre for Medium-Range Weather Forecasts (ECMWF) analyses, and surface albedo and emissivity data from the International Geosphere–Biosphere Programme global land surface classification to initialize a broadband radiative flux model known as BugsRad.

BugsRad is based on the two-stream, doubling-adding solution to the radiative transfer equation introduced by Ritter and Geleyn (1992) and assumes a plane-parallel atmosphere over the  $1.4 \text{ km} \times 1.8 \text{ km}$  *CloudSat* field of view. Molecular scattering, gaseous absorption, and absorption and scattering by both liquid and ice are all modeled in 2B-FLXHR. Molecular absorption and scattering properties computed using the correlated- $k$  formulation of Fu and Liou (1992) are combined with cloud optical properties that are based on retrieved effective radii and water contents found in *CloudSat*'s 2B-CWC product using Mie theory for liquid particles and the anomalous diffraction theory-based parameterizations of Stephens et al. (1990) and Mitchell et al. (1996) for ice. The delta-Eddington approximation is then applied over six SW bands, and a constant-hemisphere formulation is applied to 12 LW bands. These bands are appropriately weighted and combined into the two broadband flux estimates that are ultimately reported, one covering the SW from 0 to  $4 \mu\text{m}$  and the other over the LW above  $4 \mu\text{m}$ . The rate of radiative

heating in each layer follows simply by determining the net convergence or divergence of radiative energy into or out of it. The resulting set of SW and LW fluxes and heating rates are output for each *CloudSat* footprint at the maximum vertical resolution of the Cloud Profiling Radar (CPR) and the 2B-CWC product, that is, 240 m, forming the 2B-FLXHR product.

L'Ecuyer et al. (2008) found that thin high clouds and low clouds that go undetected by *CloudSat* can lead to significant errors in flux estimates and note the need for improvement in the representation of these cloud types as well as improved modeling of precipitation, as no precipitation retrieval was included in the dataset at the time. This paper seeks to address many of the shortcomings in the original 2B-FLXHR algorithm by including coincident observations from the Cloud-Aerosol Lidar with Orthogonal Polarization (CALIOP) instrument on *CALIPSO* (Winker et al. 2004, 2007) and the Moderate Resolution Imaging Spectroradiometer (MODIS) aboard *Aqua* to improve constraints on cloud and aerosol properties in surface and top-of-atmosphere (TOA) radiative flux calculations. The method used to merge the component multisensor cloud and aerosol properties to produce the new flux estimates is described in section 2. Annual mean TOA and surface radiation budgets from the resulting A-Train flux and heating rate dataset, known as 2B-FLXHR-LIDAR, are summarized in section 3, and the seasonal variations in the impacts of clouds and aerosols are quantified in sections 4 and 5. In section 6, independent comparisons with Clouds and the Earth's Radiant Energy System (CERES) TOA flux observations are provided as a sanity check and uncertainties in the approach are assessed through a comprehensive set of sensitivity studies.

## 2. The 2B-FLXHR-LIDAR algorithm

The 2B-FLXHR-LIDAR algorithm builds off the original 2B-FLXHR algorithm but takes advantage of recent improvements in cloud and precipitation products and explicitly accounts for clouds and aerosol that are not detected by *CloudSat* (Fig. 1). Cloud location is now determined from *CloudSat*'s level-2 "Radar–Lidar Cloud Geometrical Profile" product (2B-GEOPROF-LIDAR; Mace et al. 2009), and cloud properties are assigned using the *CloudSat* level-2 "Cloud Water Content (Radar Only)" product (2B-CWC-RO). If 2B-GEOPROF-LIDAR indicates a cloud is present but 2B-CWC-RO does not contain cloud microphysical information, the MODIS-based level-2 "Cloud Optical Depth" (2B-TAU) product and collocated *CALIPSO* version-3 products (Trepte et al. 2010) are used to calculate the corresponding cloud properties. All clouds detected

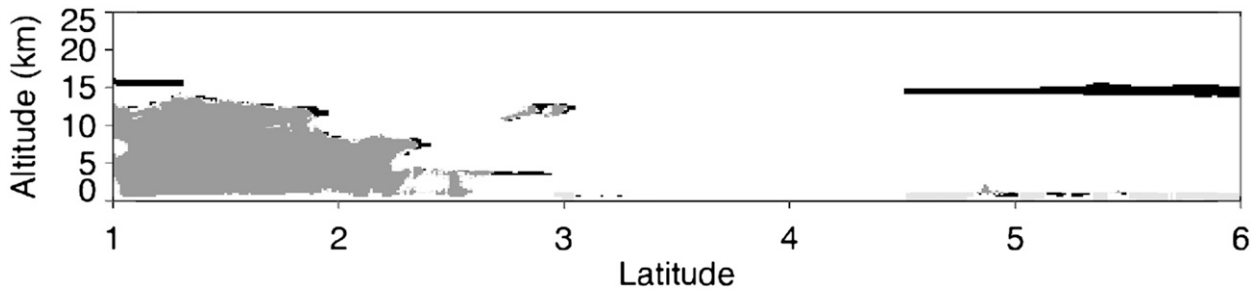


FIG. 1. Example of a cloud and aerosol mask used to illustrate *CloudSat*- and *CALIPSO*-detected clouds and aerosol. Shown are clouds from *CloudSat* (gray), clouds from *CALIPSO* (black), and aerosol from *CALIPSO* (light gray).

only by CALIOP are separated into thin ice and liquid cloud categories on the basis of temperature; mid- and low-level clouds that are warmer than 253.15 K are assumed to be liquid, and clouds that are colder than 253.15 K are assumed to be composed of all ice. The optical depths of such thin ice clouds are obtained by use of a lidar-transmission method similar to those of Comstock and Sassen (2001), Lo et al. (2006), and Haladay and Stephens (2009). The method uses ratios of measured molecular backscatter profiles from CALIOP and estimated cloud-free Rayleigh backscatter profiles to calculate optical depth. The ice water content (IWC) is then determined using

$$\tau_{\text{cloud}} = \frac{3}{2} \frac{\text{IWC}}{\rho_{\text{ice}} R_{\text{eff}}} \Delta z, \quad (1)$$

where  $\rho_{\text{ice}}$  is the density of ice and  $\Delta z$  is the thickness of the layer (Stephens 1978). The equivalent mass sphere effective radius  $R_{\text{eff}}$  is assumed to be 30  $\mu\text{m}$  for all thin ice clouds not detected by *CloudSat* from the analysis of ground-based lidar observations in L'Ecuyer et al. (2008). The impact of this assumption is shown to be much smaller than other sources of uncertainty discussed in section 6.

If the lidar-transmission method fails, the 532-nm-feature optical depth (OD) from *CALIPSO*'s "CAL\_LID\_L2\_05kmCLay" product is used as default to deduce the IWC. In the event that neither method yields a solution, an IWC of 1.5  $\text{mg m}^{-3}$  is assumed, independent of cloud temperature, loosely consistent with the analysis of the Microwave Limb Sounder reported in L'Ecuyer et al. (2008). Thin ice cloud and cirrus undetected by *CloudSat* typically have optical depths between 0.1 and 0.2; these clouds will be referred to as thin cirrus for the remainder of this paper. These values are consistent with ground-based-lidar optical-depth measurements of thin cirrus clouds ranging from 0.03 to 0.3 (Sassen et al. 2009).

CALIOP-detected low clouds are assigned optical depths and effective radii on the basis of the MODIS-based

2B-TAU product. Liquid water contents (LWC) are subsequently derived from Eq. (1), where IWC is replaced by LWC. If 2B-TAU fails, LWCs of clouds below 1 km are prescribed to have LWC of 50  $\text{mg m}^{-3}$  on the basis of the climatic values of Miles et al. (2000) and clouds above 1 km are assumed to have LWC of 120  $\text{mg m}^{-3}$  on the basis of analysis of clouds at the  $-30\text{-dBZ}$  threshold of detection of the CPR. On the basis of MODIS mean effective radii distributions, an effective radius of 13  $\mu\text{m}$  is assumed where 2B-TAU fails.

Precipitation is identified using the recently developed *CloudSat* level-2 "Precipitation Column" (2C-PRECIP-COLUMN) product (Haynes et al. 2009), which supplies cloud and rain liquid water contents (CLWC and RLWC) and produces an estimate of the expected vertical extent of rainwater in the column. The current iteration of 2C-PRECIP-COLUMN partitions cloud water and rainwater in precipitating scenes following the method of Lebsock et al. (2011), who document an approach that uses the different sensitivities of MODIS optical depth and CPR path-integrated attenuation to simultaneously infer the cloud and rainwater contents in warm-topped maritime clouds. The ratio of cloud water to rainwater is parameterized as a function of retrieved rainfall rate on the basis of the analysis of global *CloudSat* observations from 2007 by Lebsock and L'Ecuyer (2011). If the rain column exceeds the freezing level, rainwater is linearly decreased from the value at the freezing level to the reported rain-top height. Cloud water is added from the lifting condensation level to rain top in the same manner, with cloud water also decreased linearly from the freezing level to rain-top height if necessary, with cloud-droplet effective radii assumed to be 13  $\mu\text{m}$  consistent with the nonprecipitating-cloud assumption described above. In scenes in which 2C-PRECIP-COLUMN fails to retrieve rain or cloud water, climatological values are adopted. CLWC is set to 0.1  $\text{g m}^{-3}$  in each *CloudSat* bin that contains a cloud, consistent with the mean value of CLWC in 2C-PRECIP-COLUMN. If 2C-PRECIP-COLUMN classifies the pixel as rain certain but does not provide a rainfall estimate,

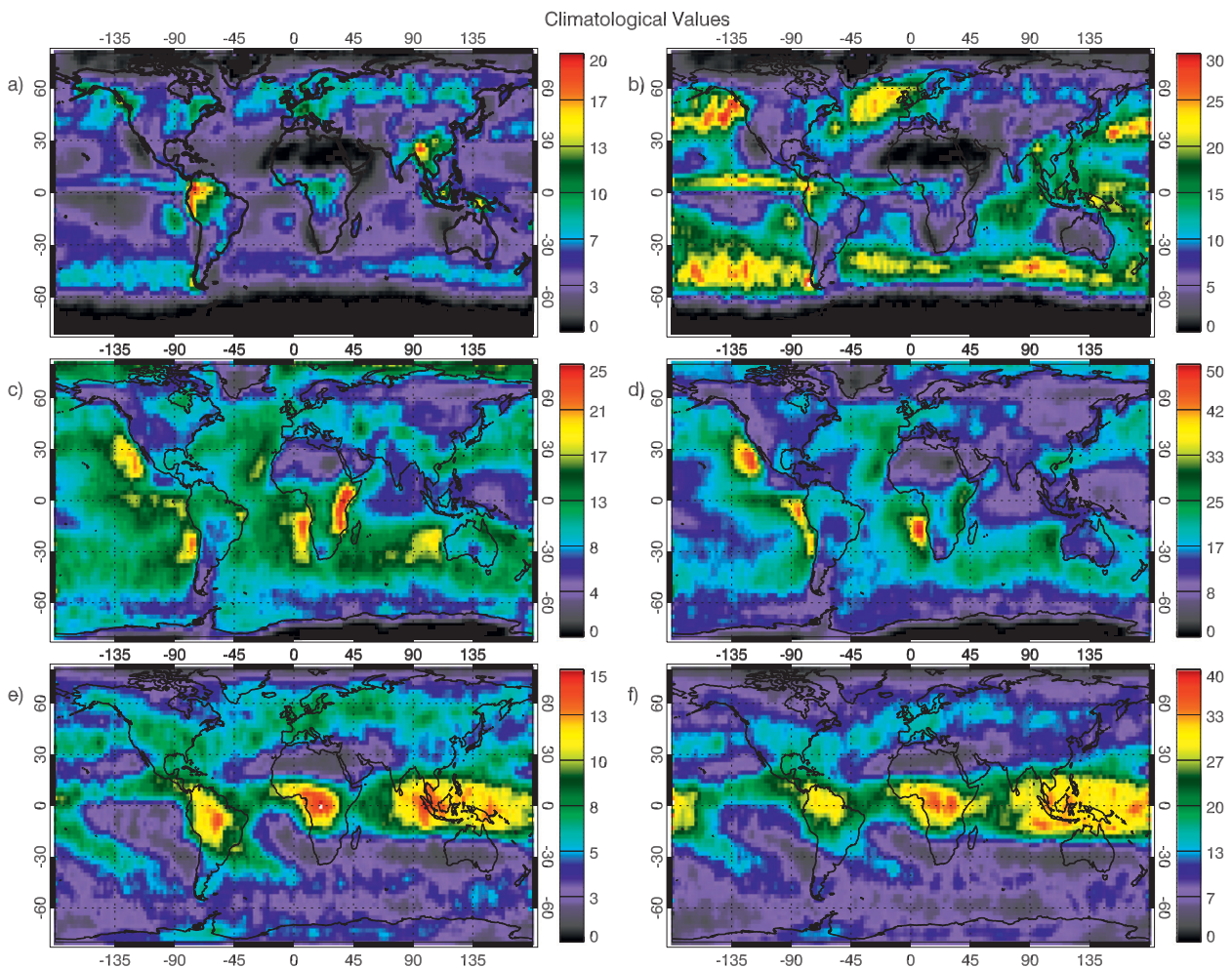


FIG. 2. Fraction of occurrence (%) for which climatological values of precipitation, low cloud, and thin cirrus cloud were used. Included are (a) climatological values for precipitation, (b) fraction of occurrence for precipitation, (c) climatological values for low cloud, (d) fraction of occurrence for low cloud, (e) climatological values for thin cirrus cloud, and (f) fraction of occurrence for thin cirrus cloud.

such as typically occurs over land because of an inability to accurately calculate path-integrated attenuation, we assume an RLWC of  $0.15 \text{ g m}^{-3}$  corresponding to a rainfall rate of  $2 \text{ mm h}^{-1}$ , the mean retrievable rainfall rate in the 2C-PRECIP-COLUMN rain-certain retrievals. Rain-probable or -possible scenes are indicative of drizzle, and a mean value for RLWC of  $0.02 \text{ g m}^{-3}$ , representative of a  $0.2 \text{ mm h}^{-1}$  drizzle rate, is assumed. Total attenuation of the CPR signal is indicative of heavy precipitation for which 2C-PRECIP-COLUMN reports a maximum retrievable rainfall rate. In such cases the RLWC is set to  $0.6 \text{ g m}^{-3}$ , which is consistent with a rainfall rate of  $10 \text{ mm h}^{-1}$  that has been shown to be the mean rain rate required to obtain agreement between bulk oceanic rainfall accumulations from *CloudSat* and the Tropical Rainfall Measuring Mission (TRMM) precipitation radar (Berg

et al. 2010; Stephens et al. 2010). Raindrop size distributions for all pixels are then derived from the Marshall-Palmer drop size distribution. These assumptions maximize the information provided by the *CloudSat* CPR in the limited number of scenes for which a quantitative retrieval of condensate is not possible, and it is demonstrated in section 6 that these assumptions, while very approximate, have a relatively small impact on the results. Note also that the addition of 2C-PRECIP-COLUMN data in 2B-FLXHR-LIDAR represents the first direct use of precipitation information in a satellite-derived radiative flux and heating-rate dataset.

The climatological values for precipitation, low cloud, and thin cirrus cloud are only used if no input data are available. Figure 2 demonstrates how often these assumptions are used to represent precipitation, low cloud, and thin cirrus cloud, along with their

respective fraction of occurrence. Climatological values are used generally less than 10% of the time for rain over ocean, less than 20% for low clouds, and less than 15% for thin cirrus clouds. Precipitation is not retrieved in cases in which low cloud is dominant and over land where the path-integrated attenuation retrieval of precipitation cannot be calculated. The majority of climatological values for low cloud and thin cirrus occur where they are most frequent; low-cloud climatological values are used near midlatitude storm tracks and subsidence regions off the west coasts of the continents, and thin cirrus is used in the tropics. On the global average, climatological values of rainfall are used in 5% of the rainfall profiles observed by *CloudSat* and climatological low and thin cirrus clouds are adopted in 9% and 4% of these cloud cases, respectively. Errors due to these assumed cloud properties are assessed in the sensitivity studies found in section 6.

The location and optical depth of aerosol layers originate from *CALIPSO* “CAL\_LID\_L2\_05kmALay” data. Aerosol species and vertical distribution are extracted from the *CALIPSO* vertical feature mask described in detail by Omar et al. (2009). Single-scatter albedo and asymmetry parameter are assigned to each aerosol layer on the basis of the 532-nm aerosol optical depth and mean radius from *CALIPSO* following the method of D’Almeida et al. (1991) and Deepak and Gerber (1983), similar to the models used by the Spectral Radiation-Transport Model for Aerosol Species (SPRINTARS) global transport model (Takemura et al. 2002). The large mode of all *CALIPSO* species that are defined to be bimodal in Omar et al. (2009) is assumed to be composed of dust particles, and the optical depth is partitioned by the volume fraction of each mode.

### 3. Flux estimates

Resulting annual-mean all-sky estimates of TOA incoming shortwave, TOA outgoing shortwave (OSR), TOA outgoing longwave (OLR), surface downwelling shortwave (SSR), surface downwelling longwave (SLR), surface upwelling reflected shortwave, and surface emission from *CloudSat* observations from June 2006 through April 2011 are shown in Fig. 3. Areas of persistent cloudiness are evident in the OSR along with deserts and areas that are frequently covered with snow or ice evident in the surface reflection. The ITCZ can be seen in OLR as a minimum across the tropics. OLR is largest in subsidence regions over open oceans where high clouds are less frequent and, especially, over warm deserts.

All-sky fluxes averaged annually for the *CloudSat* mission at the TOA and surface are summarized in Table 1. Fluxes are weighted by area for all latitudes

between 82°S and 82°N, the minimum and maximum latitudes observed by *CloudSat*, and SW fluxes are weighted [as in L’Ecuyer et al. (2008)] for each pixel in the *CloudSat* vertical profile by the average daily insolation over Earth by latitude and day of year. OSR is estimated to be 89.4 W m<sup>-2</sup>, somewhat lower than in previous observational Earth Radiation Budget (ERB) studies because of the preferential sampling of low solar zenith angles at the 1330 local time A-Train overpass, which leads to a low bias in cloud albedo. OLR is found to be 233.8 W m<sup>-2</sup>, consistent with past studies (Ellis and VonderHaar 1976; Stephens et al. 1981; Harrison et al. 1990; Rossow and Zhang 1995). The estimation of LW emission to the surface is an area of active study. A value of 351.9 W m<sup>-2</sup> is obtained from the new 2B-FLXHR-LIDAR product, closer to the more recent observational estimates (Stephens et al. 2012) than to those reported in Kiehl and Trenberth (1997) and Trenberth et al. (2009).

### 4. Cloud radiative effects

The radiative effects of all clouds included in the 2B-FLXHR-LIDAR dataset are calculated. Clouds are then separated to find the impacts on the cloud radiative effect (CRE) by clouds only detected by *CALIPSO* and undetected by *CloudSat*.

#### a. Total cloud radiative effect

The impacts of clouds on radiative fluxes can be quantified in terms of the CRE, also referred to as cloud forcing (Hartmann et al. 1986; Ramanathan et al. 1989), defined as

$$\text{CRE} = (F^\uparrow - F^\downarrow)_{\text{Clear}} - (F^\uparrow - F^\downarrow)_{\text{All-Sky}}, \quad (2)$$

where  $F^\downarrow$  and  $F^\uparrow$  are downwelling and upwelling fluxes in clear-sky and all-sky conditions, as subscripted. Total LW, SW, and net radiative effects from all clouds detected by *CloudSat* and *CALIPSO* are shown in Fig. 4, and the seasonal cycles of their zonal means are presented in Fig. 5. The ITCZ is readily evident in Fig. 4 as the maximum negative CRE in the SW. Widespread areas of low cloud, located on the western coast of the continents, are also evident features in the SW CRE. The maximum TOA LW CRE occurs in the western Pacific Ocean, and surface LW CRE is strongest in the storm tracks in both hemispheres. Overall, clouds cool Earth by 18.1 W m<sup>-2</sup> on annual average, reflecting 45.3 W m<sup>-2</sup> and retaining 27.2 W m<sup>-2</sup> (Table 2). These results lie between previous estimates from Harrison et al. (1990) and Raschke et al. (2005) who find total

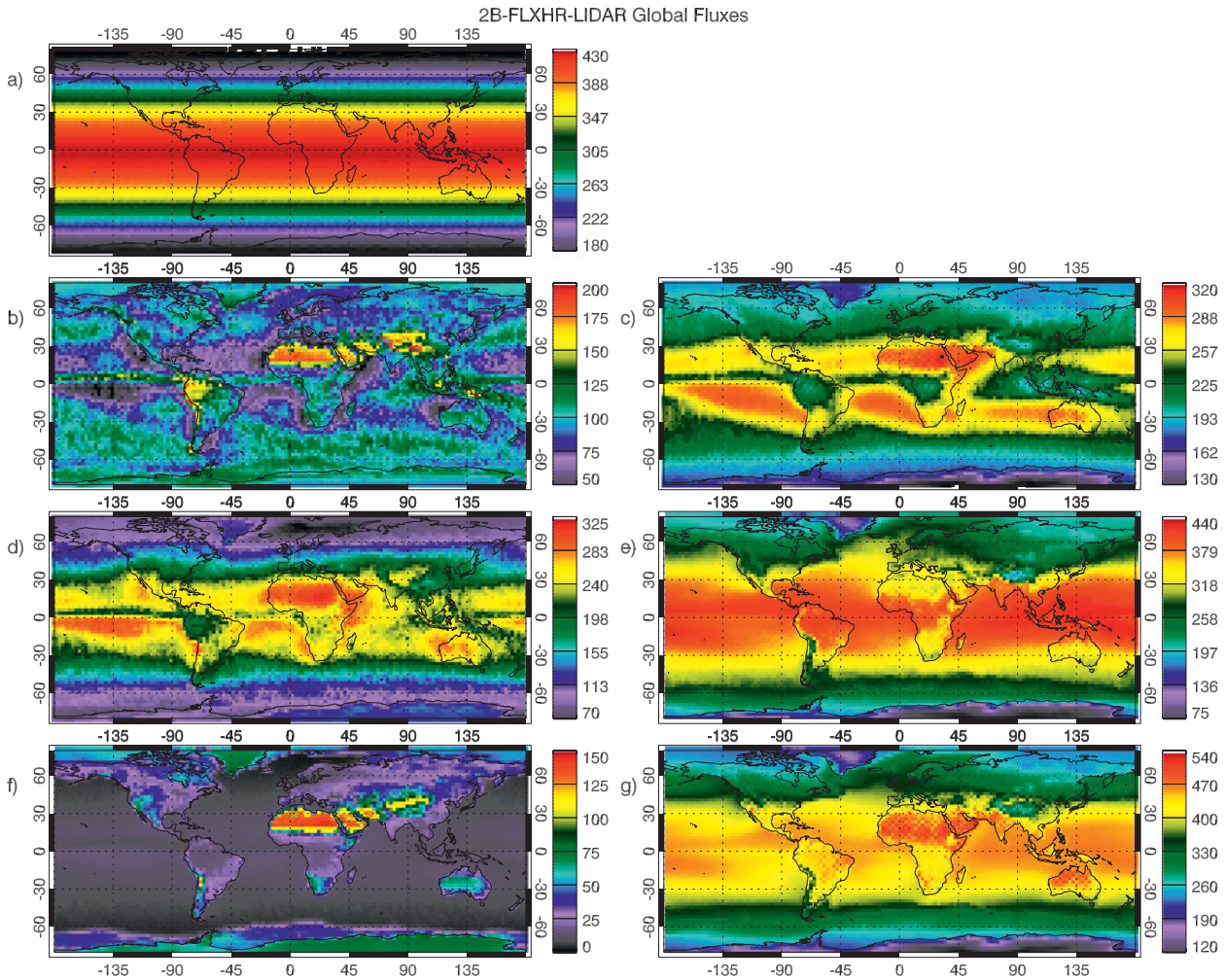


FIG. 3. Annual all-sky radiative fluxes ( $\text{W m}^{-2}$ ) for (a) TOA incoming SW, (b) OSR, (c) OLR, (d) SSR, (e) SLR, (f) surface upwelling reflected SW, and (g) surface emission.

CREs of  $-17$  and  $-24 \text{ W m}^{-2}$  using ERB Experiment and International Satellite Cloud Climatology Project data, respectively. Note that errors in global cloud-forcing estimates are extremely difficult to assess because of the need to account for uncertainties in clear-sky radiative fluxes, to represent errors in the specification of cloud properties, and to distinguish random errors from systematic errors. Upper bounds on the errors due to various factors that contribute to cloud-forcing uncertainty are summarized in Tables 6 and 7 (described in detail in section 6b below), but with incomplete knowledge of correlations between these sources of error as well as the relative magnitude of their random and systematic components, they cannot be readily combined to yield an overall estimate of cloud-forcing error. Instead we report relative differences in cloud-forcing estimates between 2B-FLXHR-LIDAR and those derived from CERES TOA fluxes partitioned into clear-sky

and all-sky components. Although such comparisons do not provide a true error estimate, they do yield a useful baseline given the very different approaches from which these cloud-forcing estimates derive. For similar reasons, errors in surface cloud forcing cannot be assessed at this time.

TABLE 1. Globally and annually averaged TOA and surface (SFC) fluxes ( $\text{W m}^{-2}$ ) from the 2B-FLXHR-LIDAR product. Uncertainties are calculated using the uncertainty analysis found in section 6. This includes the sensitivity study, the differences between the 2B-FLXHR-LIDAR product and TOA and surface flux estimates from the CERES product, and estimates of uncertainties in the prescribed surface emissivity and albedo.

	$F_{\text{LW}}^{\downarrow}$	$F_{\text{LW}}^{\uparrow}$	$F_{\text{SW}}^{\downarrow}$	$F_{\text{SW}}^{\uparrow}$
TOA	—	$233.8 \pm 5$	$341.3 \pm 0.5$	$89.4 \pm 7$
SFC	$351.9 \pm 10$	$399.8 \pm 10$	$189.8 \pm 13$	$22.3 \pm 3$

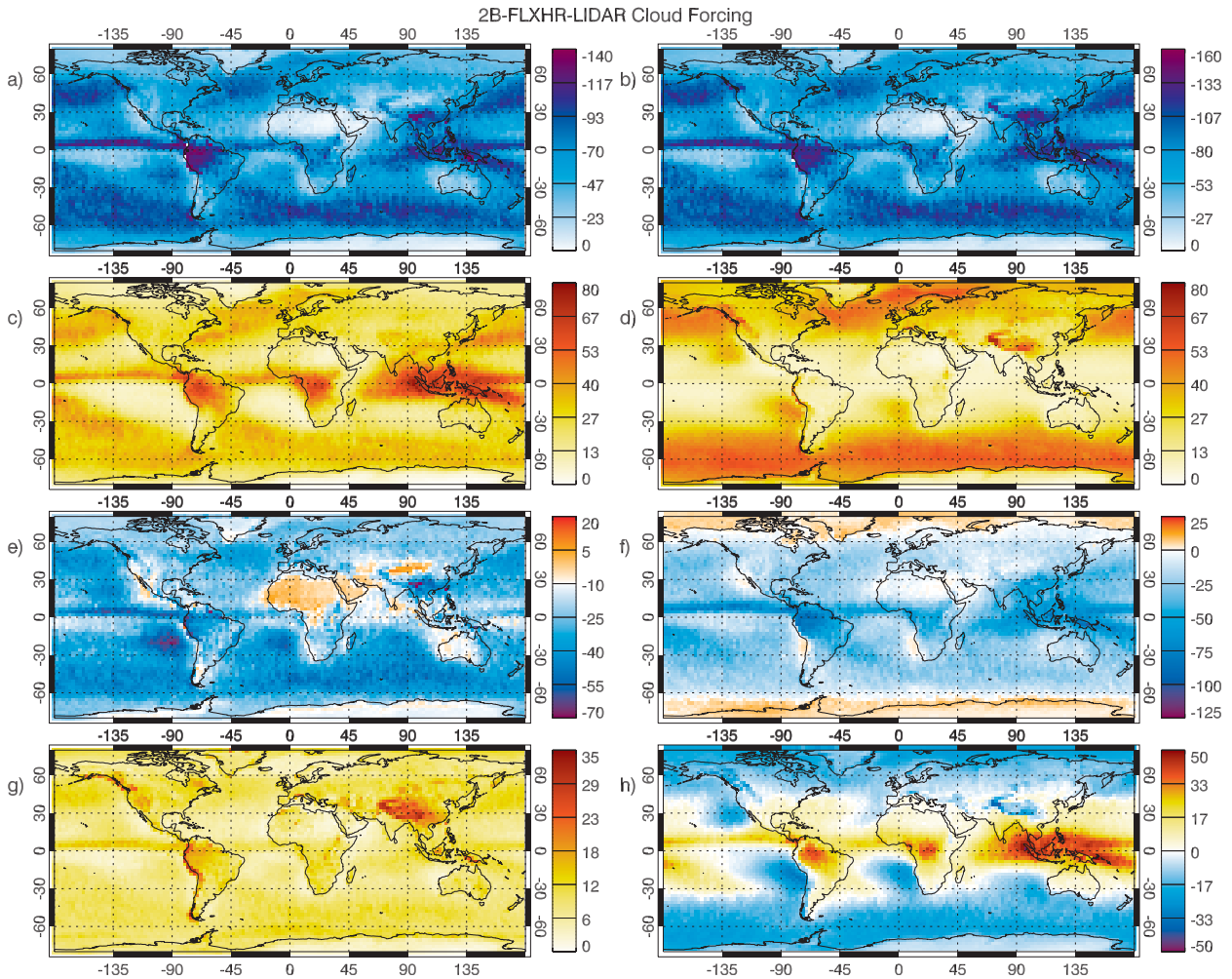


FIG. 4. The annual mean radiative effects ( $\text{W m}^{-2}$ ) of all clouds detected by *CloudSat* and *CALIPSO*: (a) TOA SW, (b) surface SW, (c) TOA LW, (d) surface LW, (e) TOA net, (f) surface net, (g) atmospheric CRE for SW, and (h) atmospheric CRE for LW.

Taking the difference of the TOA and surface cloud forcing yields the cloud impact on atmospheric radiative heating. Globally in the SW, clouds warm the atmosphere with a mean radiative warming of  $7.0 \text{ W m}^{-2}$ . Overall in the LW, clouds warm the atmosphere by  $1.6 \text{ W m}^{-2}$ , but not uniformly. The warming is focused near the tropics where cloud thickness tends to be larger, whereas the mid- and upper-latitude clouds tend to contribute radiative cooling that nearly balances the warming in the tropics.

On a zonal basis, seasonal variability is relatively small in the tropics, with regional differences influenced by the location of the ITCZ. Bimodal peaks in the TOA LW CRE, for example, track the shift in the ITCZ between the hemispheres. Shortwave CRE variations in the midlatitudes are dominated by variations in incoming solar radiation. Shortwave effects vanish in the winter-hemisphere polar regions, leading to positive net

CRE as LW effects dominate. Increased SW cloud forcing during the summer, in the midlatitudes, corresponds to clouds in midlatitude storm tracks that are brighter because of increased cloud albedo, from illumination at higher solar zenith angles, and they tend to be more frequent in the Southern Hemisphere.

#### b. Impacts of CALIOP clouds undetected by CloudSat

To assess and document the influence of CALIOP and MODIS data on the 2B-FLXHR product, it is instructive to examine the radiative impacts of low and high clouds undetected by *CloudSat*. Figures 6 and 7 illustrate the CRE of undetected low and high clouds, partitioned into liquid and ice clouds on the basis of a temperature threshold of 253.15 K as noted above, annually averaged over the *CloudSat* mission. Undetected low clouds exert a strong cooling effect,

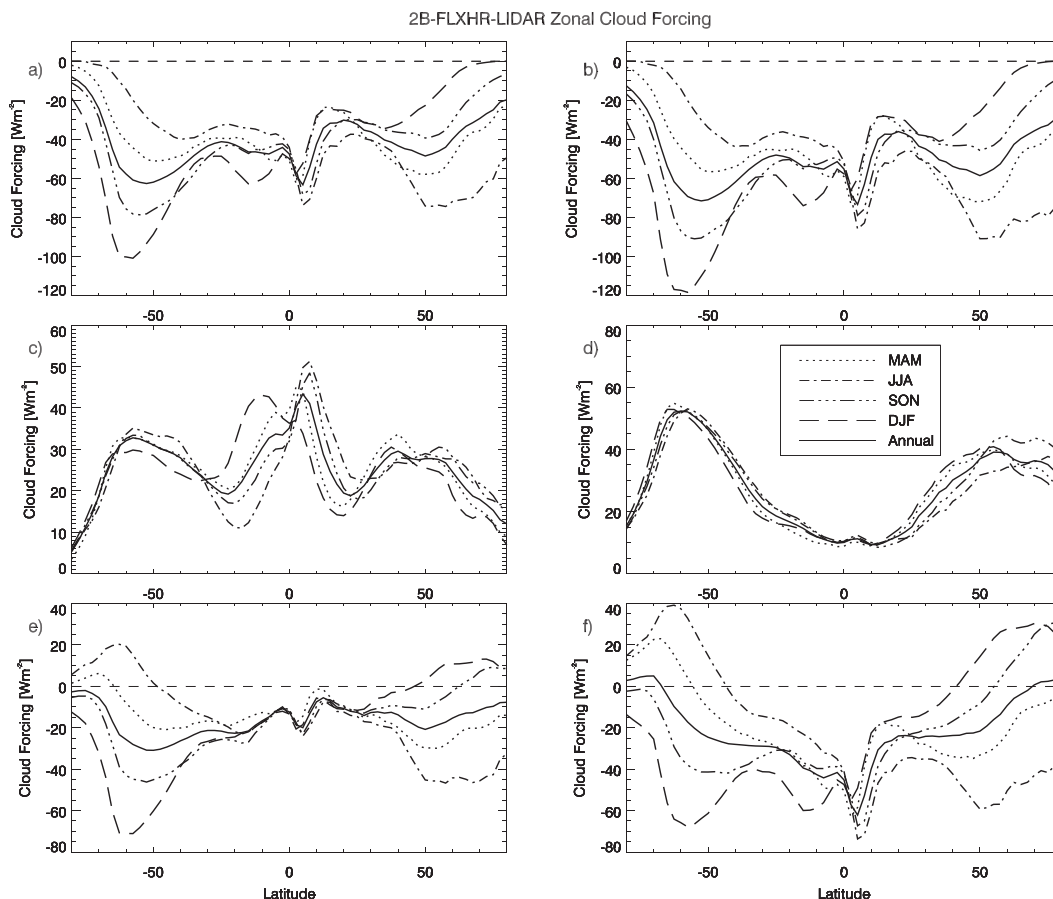


FIG. 5. Zonally averaged annual and seasonal radiative effects ( $\text{W m}^{-2}$ ) for all clouds detected by *CloudSat* and *CALIPSO*: (a) TOA SW, (b) surface SW, (c) TOA LW, (d) surface LW, (e) TOA net, and (f) surface net CRE. Seasons are defined as December–February (DJF), March–May (MAM), June–August (JJA), and September–November (SON).

particularly over dark ocean areas. Surface warming near the poles is observed for surface net CRE as low clouds have a strong impact in the LW during the winter. Undetected cirrus clouds have a much smaller radiative effect than low clouds because of their small optical depths ( $\ll 1$ ) and composition of sparse ice crystals, which are not efficient at absorbing or reflecting SW radiation but are effective absorbers of LW radiation (Stephens 1980).

On a regional basis, undetected low clouds exhibit their strongest impacts in three major subsidence zones near the west coasts of North America, South America, and southern Africa, where SW CRE from the undetected low clouds can reach  $-45 \text{ W m}^{-2}$ . Longwave radiation at the surface is also enhanced in these regions by emission from cloud water. For undetected cirrus, positive radiative effects at the TOA are strongest close to the ITCZ and the western Pacific where deep convection is frequent.

Seasonal, zonal-averaged impacts of clouds not detected by *CloudSat* are presented in Figs. 8 and 9, and global statistics are summarized in Table 3. Undetected low clouds exhibit the highest zonal impacts at higher latitudes, in both hemispheres, associated with storm

TABLE 2. Seasonal and annual globally averaged CREs ( $\text{W m}^{-2}$ ) of clouds detected by *CloudSat* and *CALIPSO*. Relative differences in all-sky and clear-sky fluxes between 2B-FLXHR-LIDAR and CERES TOA are used to establish approximate error bounds on TOA CRE estimates.

	DJF	MAM	JJA	SON	Annual
$\text{TOA}_{\text{SW}}$	-46.9	-43.5	-43.9	-46.2	$-45.3 \pm 3.2$
$\text{TOA}_{\text{LW}}$	25.4	28.0	27.0	26.4	$27.2 \pm 1.9$
$\text{TOA}_{\text{NET}}$	-20.5	-15.5	-16.9	-19.8	$-18.1 \pm 3.7$
$\text{SFC}_{\text{SW}}$	-54.2	-50.6	-50.5	-53.0	-52.3
$\text{SFC}_{\text{LW}}$	26.6	25.7	23.9	26.1	25.6
$\text{SFC}_{\text{NET}}$	-28.5	-26.1	-25.3	-26.9	-26.7

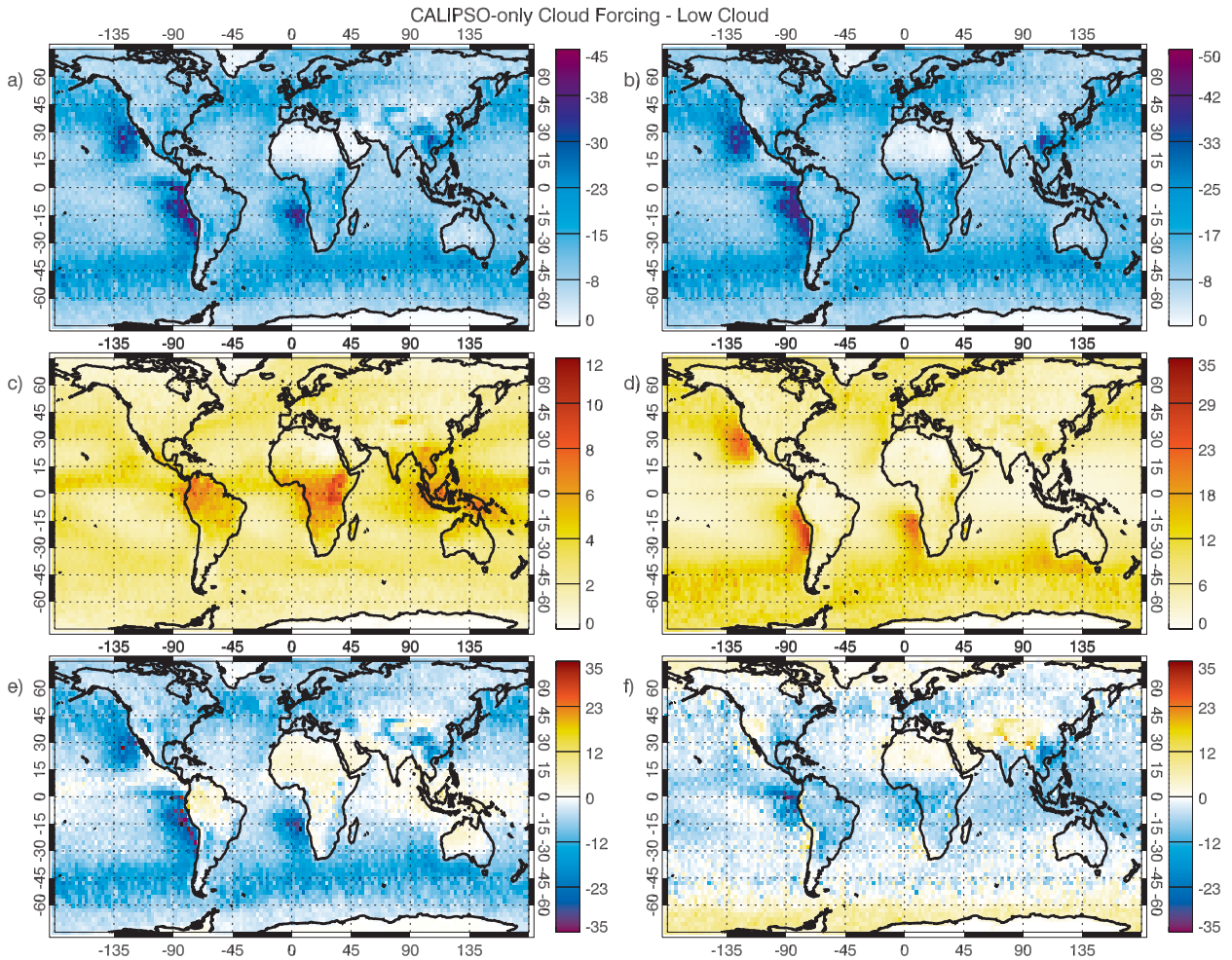


FIG. 6. The annual mean radiative effects ( $\text{W m}^{-2}$ ) of low clouds undetected by *CloudSat*: (a) TOA SW, (b) surface SW, (c) TOA LW, (d) surface LW, (e) TOA net, and (f) surface net.

tracks. The undetected low clouds impose a net negative effect at the TOA, further cooling the atmosphere by reflecting more SW radiation. Cooling is found at the surface as well, with the exception of a small net positive effect closer to the poles in the winter hemisphere where increased emission from low clouds dominates. Globally and annually, undetected low clouds impact the net TOA fluxes by  $-4.1 \text{ W m}^{-2}$  and net surface fluxes by  $-1.2 \text{ W m}^{-2}$ . Undetected cirrus exhibit little effect in higher latitudes and midlatitudes, with a maximum effect near the tropics. The TOA LW effect can be as large as  $3.3 \text{ W m}^{-2}$  zonally, but the global mean effect is an addition of  $1.1 \text{ W m}^{-2}$ .

## 5. Aerosol direct effect

Previous satellite-based estimates of the radiative effects of aerosols, known as the direct effect, employ data

from passive sensors that are generally limited to oceans and clear skies and do not account for the effects of vertical layering of aerosols (Remer and Kaufman 2006; Yu et al. 2006; Zhang et al. 2005). The advantage of merging multiple A-Train datasets is that we can quantify the effects of aerosols on atmospheric radiation by explicitly modeling the effects of aerosol relative to locations of clouds. The vertical profiles of aerosol layers provided by CALIOP allow the reflective and absorptive properties of each aerosol to be specified in each cloud-free atmospheric layer.

For this study, the direct effect of aerosol is defined as the SW flux difference between including *CALIPSO*-detected aerosol and no aerosol at all at the TOA or the surface. The annual and seasonal direct effects of aerosols are illustrated in Fig. 10. Mineral dust dominates from the western coast of India through dust-transport regions over the Atlantic Ocean. The seasonal shift of

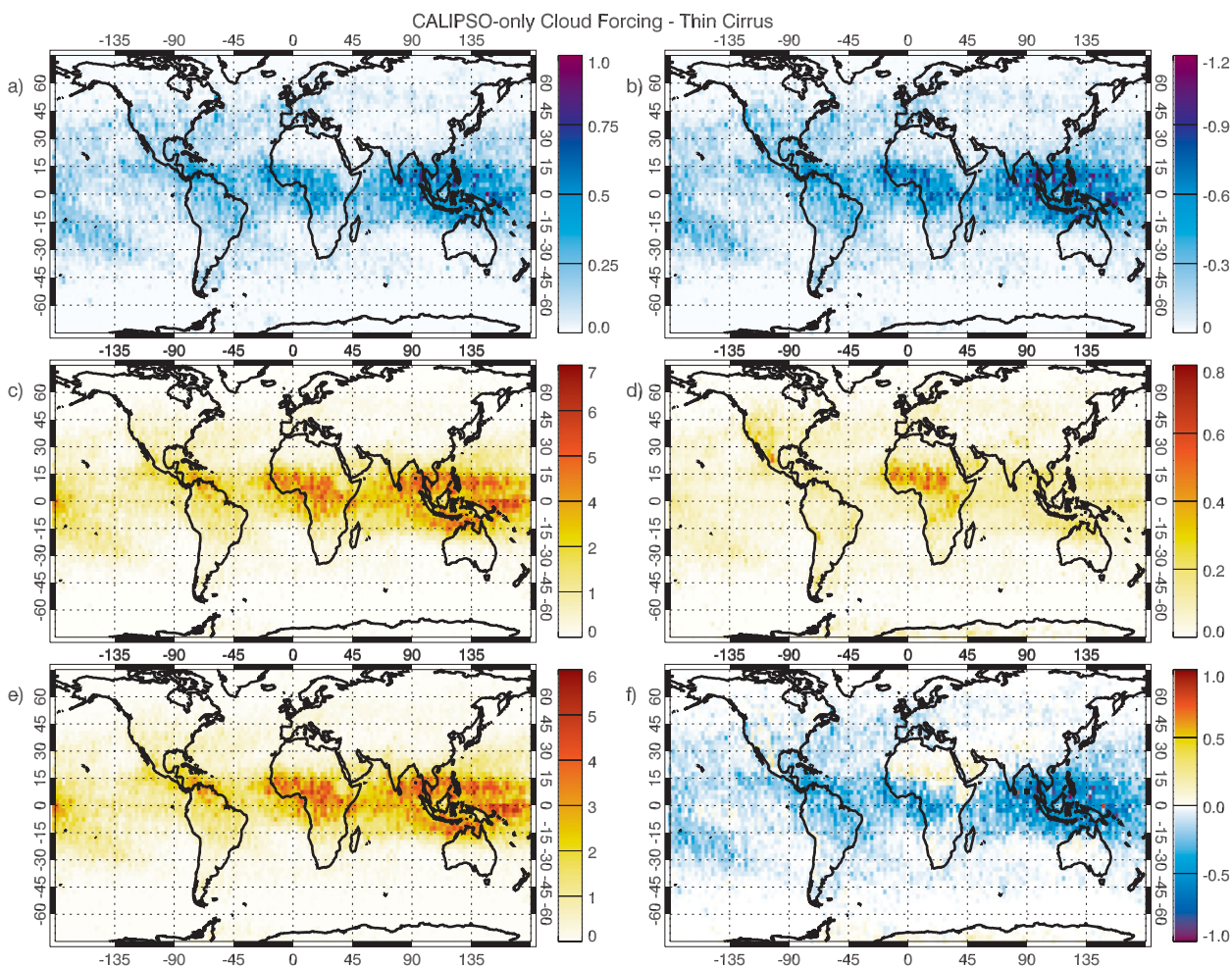


FIG. 7. As in Fig. 6, but for thin cirrus clouds undetected by *CloudSat*.

Saharan dust transport can be seen, and the most evident effects are in the spring and summer months. Dust increases outgoing SW over the oceans but dims the desert regions. Positive forcing is also observed in areas of heavier biomass burning in southern Africa in September–November (SON). Here smoke is frequently lofted above clouds, reducing their albedo, similar to the findings of Chand et al. (2009). Surface cooling in SON and December–February (DJF) is evident in southern and eastern Asia and is caused by haze, pollution, and dust advected into these regions.

Effects of aerosol can best be compared with other studies by looking at their global impacts (Table 4). The combination of *CloudSat* and *CALIPSO* data allows the direct effect to be quantified in clear sky and cloudy skies separately. The use of 2B-GEOPROF-LIDAR ensures only clear-sky cases, resulting in no cloud contamination. The effect of aerosol on clear-sky outgoing SW radiation over oceans is found to be  $-2.5 \text{ W m}^{-2}$ .

According to the Intergovernmental Panel on Climate Change Fourth Assessment Report (AR4), which uses some results from Yu et al. (2006), the average clear-sky over-ocean impact at the TOA is  $-5.4 \text{ W m}^{-2}$ . The AR4 results are derived from satellite sensors using passive sensor data and do not include model results listed in Yu et al. (2006). Model averages range from  $-1.7$  to  $-4.1 \text{ W m}^{-2}$ , closer to the 2B-FLXHR-LIDAR estimate presented here. This suggests that observational estimates that are based exclusively on passive sensors without explicit information about the vertical distribution of cloud and aerosol layers may overestimate the aerosol direct effect. The overestimation of the direct effect from passive sensors could be attributed to cloud contamination adding errors up to 10%–30% (Loeb and Kato 2002; Kittaka et al. 2005; Kaufman et al. 2005) and even higher, depending on how the clear scenes are defined (Remer and Kaufman 2006).

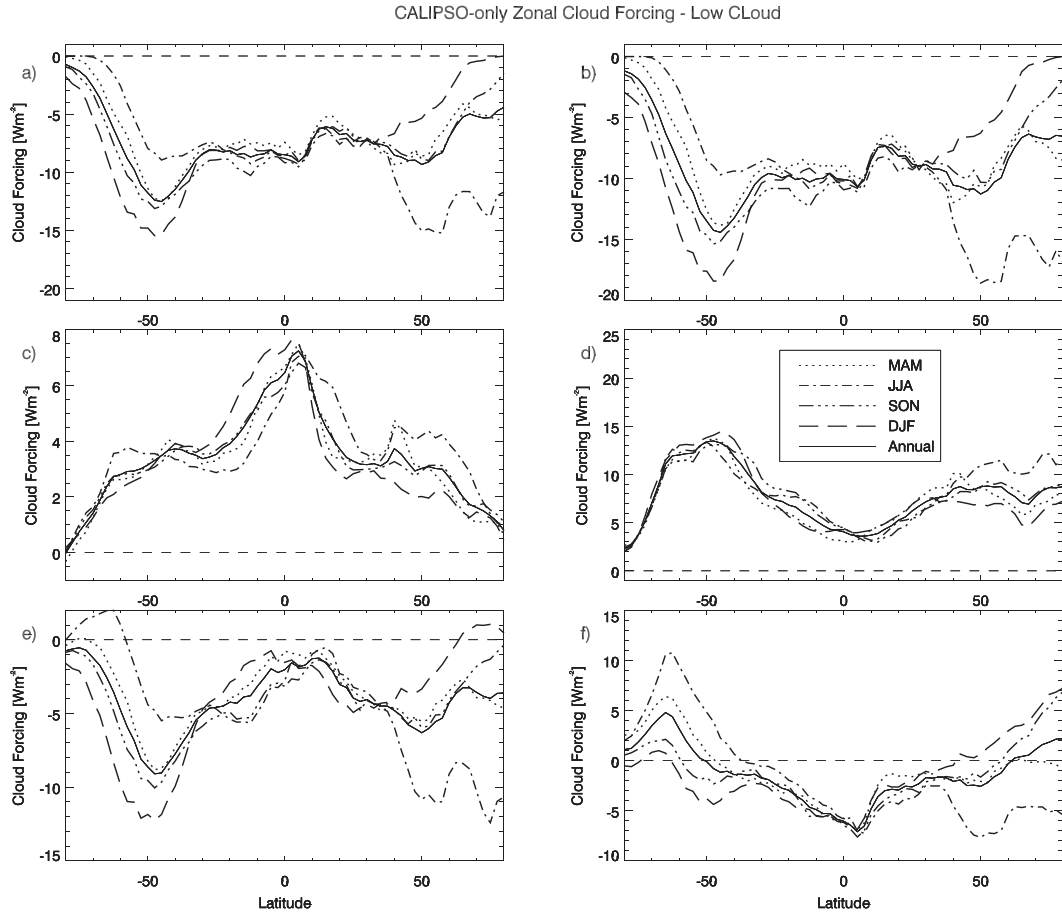


FIG. 8. As in Fig. 5, but for low clouds undetected by *CloudSat*.

Aerosols absorb and reflect incoming solar radiation, resulting in higher surface effects of aerosol relative to those at the TOA, cooling the surface by  $4.0 W m^{-2}$  globally. Global TOA radiative effects decrease relative to those over ocean only because of the positive effect of aerosol over landmasses and decrease further for all sky as aerosols dim clouds below them. Globally over land and ocean, the all-sky TOA radiative effect is  $-1.6 W m^{-2}$ , which is  $0.9 W m^{-2}$  less of an effect than that of clear sky over the ocean. The surface aerosol effect over land and ocean, however, increases relative to that over ocean only to  $-6.2 W m^{-2}$  for clear skies and  $-6.3 W m^{-2}$  for all sky.

The impacts of uncertainties in *CALIPSO* aerosol products are assessed through four sensitivity studies: 1) *CALIPSO* aerosol optical depths (AOD) are perturbed by a factor of 2 loosely based on results found by Kittaka et al. (2011), 2) all aerosols are changed to smoke with the exception of marine aerosol, 3) all aerosols are changed to dust with the exception of marine aerosol, and 4) smoke aerosols are assumed to be dust. These cases represent

extreme scenarios, but together the results provide an upper bound on the potential errors in both the magnitude of AODs and the ability to discriminate the impacts of different aerosol species on simulated fluxes.

Replacing aerosol optical properties with those of smoke results in a decrease in OSR by  $0.6 W m^{-2}$  and decreases SSR nearly  $2 W m^{-2}$  because of enhanced absorption by black carbon aerosols relative to dust. Assuming dustlike optical properties brightens aerosol layers, increasing OSR by  $0.5 W m^{-2}$  and SSR by  $0.7 W m^{-2}$ . Changing only smoke aerosol to dust also increases OSR and SSR by  $0.2 W m^{-2}$  and  $0.6 W m^{-2}$ , respectively. Altering the AOD leads to uncertainties of  $\sim 0.6 W m^{-2}$  in outgoing SW radiation and uncertainties at the surface of  $\sim 2.2 W m^{-2}$ . By combining the mean sensitivities to AOD and aerosol type (assuming these sources have approximately independent effects on accuracy) we obtain an error estimate of  $\pm 0.8 W m^{-2}$  in our estimate of TOA SW direct effect. This effectively results in a range from  $-1.7$  to  $-3.3 W m^{-2}$  for the TOA SW aerosol direct effect in clear skies over oceans.

CALIPSO-only Zonal Cloud Forcing - Thin Cirrus

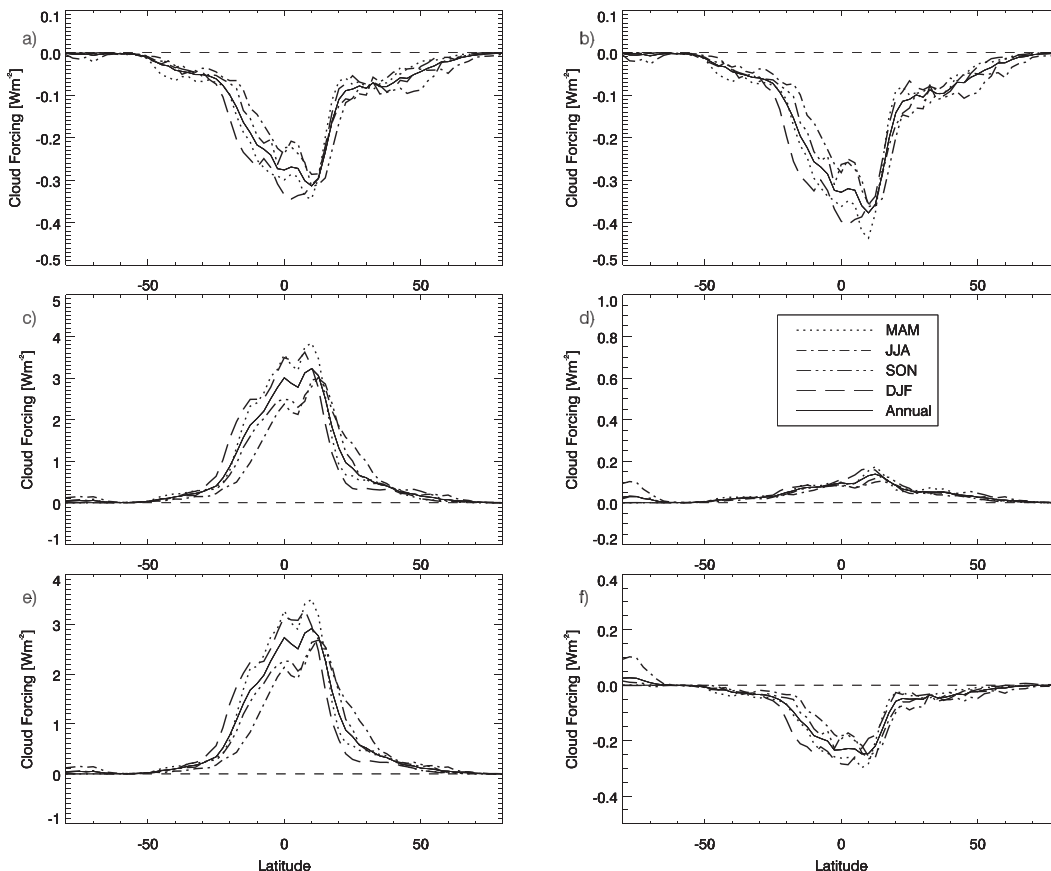


FIG. 9. As in Fig. 5, but for thin cirrus clouds undetected by *CloudSat*.

**6. Uncertainty estimates**

Uncertainties in the 2B-FLXHR-LIDAR product are assessed through a comprehensive series of sensitivity studies in which errors in input parameters are propagated through the algorithm to establish error bounds due to all relevant assumptions. Complementary comparisons with CERES TOA fluxes provide a sanity check on these error bounds and help to establish the dependence of these errors on the spatial/temporal averaging scale.

*a. Comparisons with CERES*

The CERES instrument aboard *Aqua* provides useful independent measurements of TOA and surface fluxes with which those calculated from 2B-FLXHR-LIDAR can be compared. The *Aqua* satellite orbits closely with *CloudSat*, and therefore each instrument views nearly the same clouds, surfaces, and atmospheric conditions. Although CERES has a larger field of view in comparison with *CloudSat*, a study by Kato et al. (2011) demonstrated the differences between CERES and *CloudSat*/*CALIPSO* cloud fraction decrease when averaged over area and time. Therefore direct comparisons of

TOA and surface fluxes are possible on reasonably large time and space scales. Fluxes from 2B-FLXHR-LIDAR are evaluated against the CERES fast longwave and shortwave flux (FLASHFlux) product (Stackhouse et al. 2006) in  $5^\circ \times 5^\circ$  latitude–longitude bins by collocating

TABLE 3. Seasonal and annual globally averaged CREs ( $W m^{-2}$ ) of low and high clouds undetected by *CloudSat*. Here, NS indicates a negligible difference.

	DJF	MAM	JJA	SON	Annual
Low					
TOA <sub>SW</sub>	-8.0	-8.2	-7.9	-9.2	-8.4
TOA <sub>LW</sub>	4.2	4.3	4.5	4.2	4.3
TOA <sub>NET</sub>	-4.2	-3.9	-3.4	-5.0	-4.1
SFC <sub>SW</sub>	-9.1	-8.9	-9.6	-10.0	-9.3
SFC <sub>LW</sub>	7.9	7.8	8.5	8.4	8.1
SFC <sub>NET</sub>	-1.2	-1.1	-0.9	-1.6	-1.2
High					
TOA <sub>SW</sub>	-0.2	-0.2	-0.2	-0.2	-0.2
TOA <sub>LW</sub>	1.2	1.2	1.0	1.1	1.1
TOA <sub>NET</sub>	-1.0	-1.0	-0.8	-0.9	-0.9
SFC <sub>SW</sub>	-0.2	-0.2	-0.2	-0.2	-0.2
SFC <sub>LW</sub>	0.1	0.2	0.2	0.2	0.2
SFC <sub>NET</sub>	-0.1	NS	NS	NS	NS

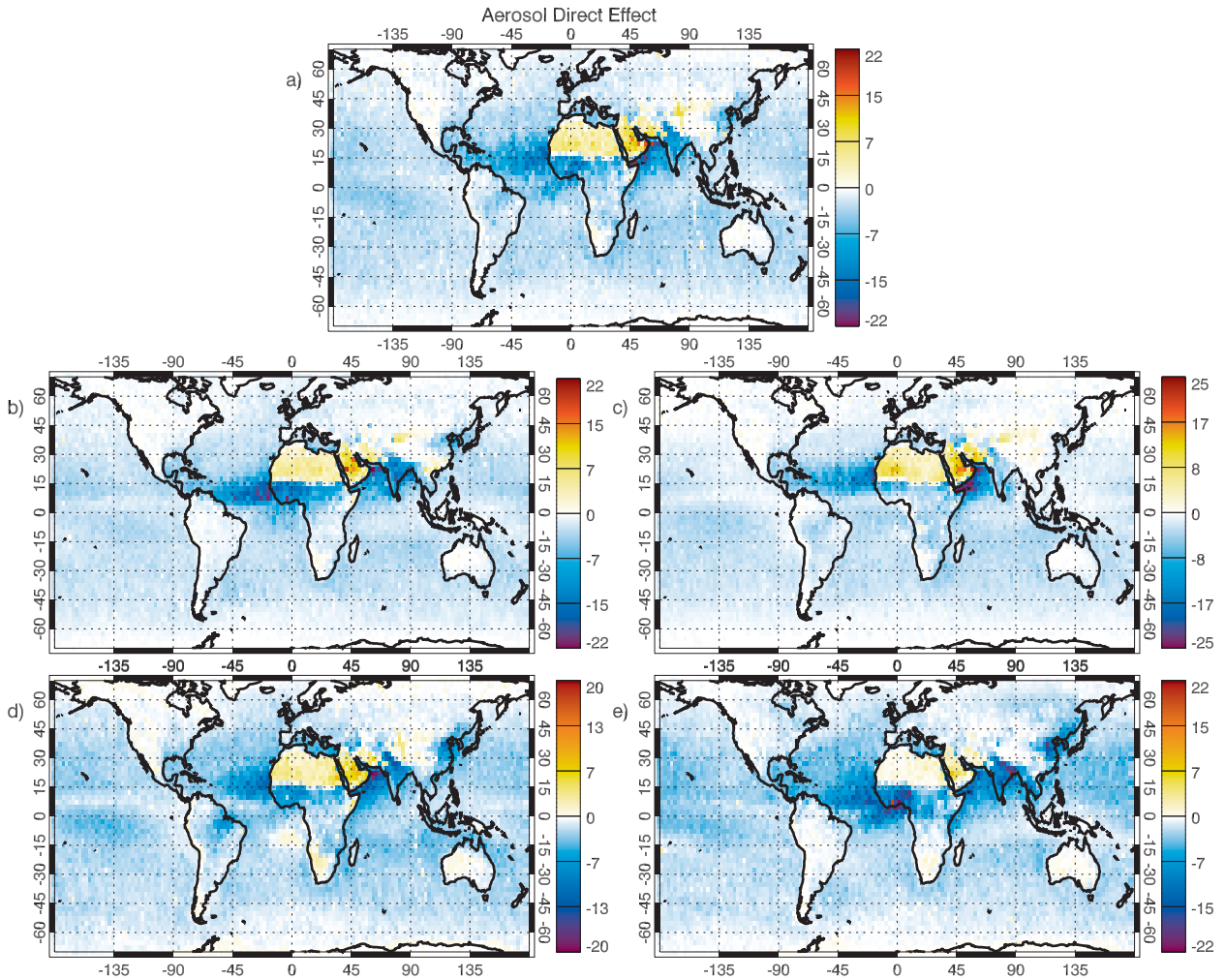


FIG. 10. (a) The global annual aerosol direct effect for all-sky conditions for the *CloudSat* mission ( $W m^{-2}$ ). The data are also divided seasonally into (b) MAM, (c) JJA, (d) SON, and (e) DJF.

each *CloudSat* footprint to the CERES footprint that is nearest to the *CloudSat* swath. On average, 21 *CloudSat* vertical profiles are collocated to an individual CERES footprint. Comparisons of all monthly  $5^{\circ} \times 5^{\circ}$  OSR, OLR, SSR, and SLR estimates from January 2007 through February 2008 are shown in Fig. 11.

RMS differences in outgoing radiation are  $5.7 W m^{-2}$  for the LW and  $16.5 W m^{-2}$  in the SW. Higher RMS differences in OSR are likely due to cloud-detection differences between the two instruments, and systematic OSR differences are much smaller at  $4.1 W m^{-2}$ . Outgoing LW is consistently lower relative to CERES, with a bias of  $-4.9 W m^{-2}$ . When one compares differences in OSR from 2B-FLXHR (L'Ecuyer et al. 2008) and from 2B-FLXHR-LIDAR, the bias decreased by  $1.4 W m^{-2}$  and RMS decreased by  $10.1 W m^{-2}$ . The increased scatter and slightly increased biases, relative to 2B-FLXHR, in SSR are likely caused by the introduction of CALIOP low

clouds, some of which were assigned properties on the basis of climatological values. Excluding CALIOP low clouds reduces the RMS difference to  $16.1 W m^{-2}$ , which is much closer to the value found using 2B-FLXHR. Surface values for LW radiation are higher than those of CERES, with a bias of  $3.8 W m^{-2}$ . Differences at the surface can result from cloud thickness assumptions in CERES, where only cloud-top pressure can be retrieved, along with the large amounts of missing data reported in

TABLE 4. The TOA and SFC direct effect ( $W m^{-2}$ ) of aerosols for the *CloudSat* mission. Clear-sky and all-sky aerosol radiative effects are shown for comparison, and global and ocean-only results are presented for comparison with passive techniques.

	Clear <sub>Ocean</sub>	All-sky <sub>Ocean</sub>	Clear <sub>Land+Ocean</sub>	All-sky <sub>Land+Ocean</sub>
TOA	-2.5	-2.0	-2.2	-1.6
SFC	-4.0	-4.1	-6.2	-6.3

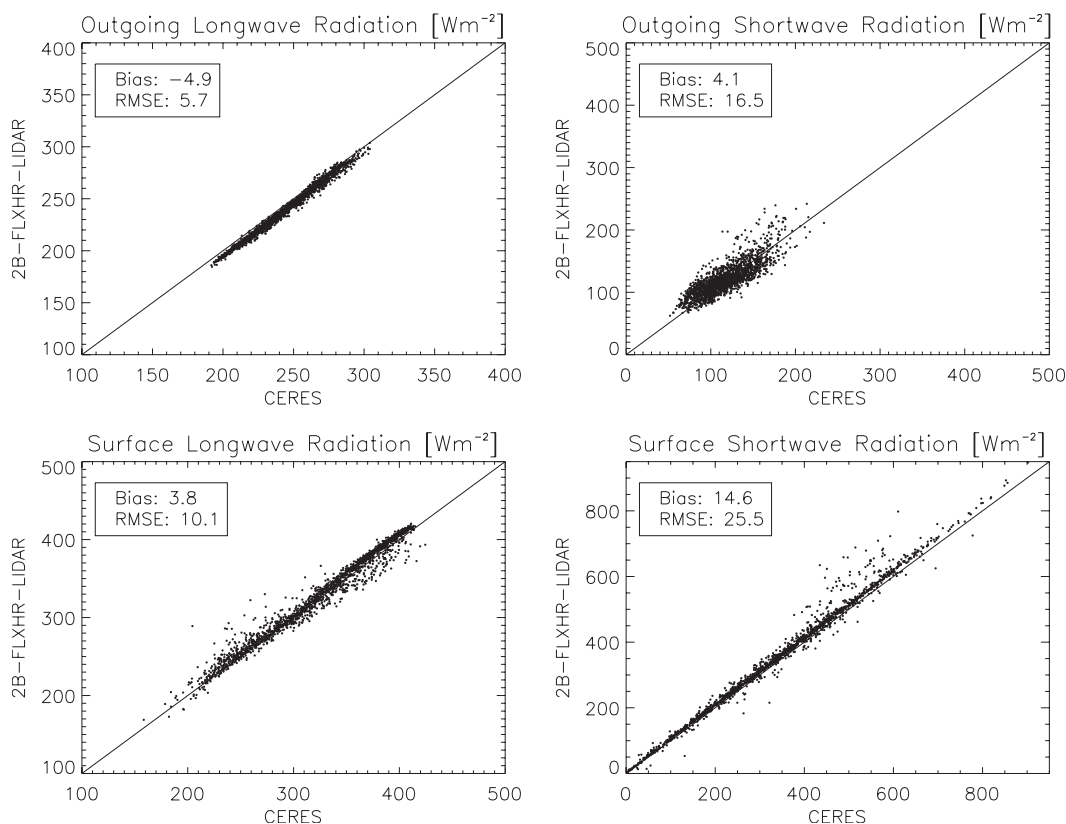


FIG. 11. Comparison of the fluxes from 2B-FLXHR-LIDAR with the CERES FLASHFlux product from January 2007 to February 2008. Each point represents an averaged  $5^{\circ} \times 5^{\circ}$  latitude-longitude grid box and contains OSR, OLR, SSR, and SLR.

CERES surface fluxes, thus decreasing the sample size in many cases by nearly 85%.

The intention of creating a product such as 2B-FLXHR-LIDAR is to apply its data over varying domain sizes and time scales. L'Ecuyer et al. (2008) showed that the uncertainties in 2B-FLXHR fluxes decrease significantly for longer-time-scale averages. Differences in 2B-FLXHR-LIDAR TOA relative to CERES fluxes on time scales of 5 days, 1 month, and 1 year and spatial resolutions of  $2^{\circ}$ ,  $5^{\circ}$ , and  $10^{\circ}$  are shown in Table 5. Bias in the LW is nearly independent of time scale, but bias decreases in the SW with increasing spatial averaging scale. RMS differences significantly decrease when time and grid size are increased. RMS differences in  $2^{\circ}$  OSR estimates, for example, decrease from  $45.7 \text{ W m}^{-2}$  for 5-day averages to  $19.4 \text{ W m}^{-2}$  for annual averages. These results suggest it is important to consider the magnitude of the signals relative to RMS differences appropriate for the time-space scale of interest when interpreting 2B-FLXHR-LIDAR analyses. When using the data on smaller scales or shorter periods, uncertainty due to cloud, aerosol, or atmospheric properties may be significant, but these instantaneous errors cancel over longer time scales.

### b. Sensitivity studies

To more rigorously attribute flux uncertainties to the specific components of the 2B-FLXHR-LIDAR algorithm, data from August 2007 are used to complete multiple sensitivity studies representing the impacts of uncertainties in atmospheric, cloud, and surface properties on LW and SW fluxes at the TOA and surface. These studies are summarized in Tables 6 and 7. In the tables, each row describes the variable examined, by how much it is perturbed for every vertical *CloudSat*

TABLE 5. Bias and RMS (in parentheses) differences ( $\text{W m}^{-2}$ ) between 2B-FLXHR-LIDAR and CERES over a range of time and spatial scales for SW and LW fluxes.

	5 day	1 month	1 year
SW			
$2^{\circ}$	7.7 (45.7)	5.5 (31.3)	4.4 (19.4)
$5^{\circ}$	6.5 (37.4)	5.2 (20.4)	4.1 (16.5)
$10^{\circ}$	6.0 (24.1)	4.9 (15.8)	3.7 (14.8)
LW			
$2^{\circ}$	-5.3 (11.8)	-5.2 (7.7)	-4.9 (5.9)
$5^{\circ}$	-5.3 (9.1)	-5.1 (6.6)	-4.9 (5.7)
$10^{\circ}$	-5.2 (6.3)	-5.0 (5.8)	-4.4 (5.0)

TABLE 6. Sensitivity of 2B-FLXHR-LIDAR TOA and surface LW fluxes to uncertainties in input variables for August 2007. Since the effect of some parameters is nonlinear, the impacts of both upward and downward perturbations are reported ( $\text{W m}^{-2}$ ). All fluxes represent the average over the *CloudSat* domain from 82°N to 82°S. The increase and decrease of each perturbation are separated by a slash, and errors displayed as NS indicate a negligible sensitivity.

Parameter	Perturbation	$\Delta F_{\text{LW,TOA}}^{\uparrow}$	$\Delta F_{\text{LW,SFC}}^{\uparrow}$	$\Delta F_{\text{LW,SFC}}^{\downarrow}$
<i>CloudSat</i> -only properties				
Precipitation	2×/none	NS/NS	NS/NS	0.1/−0.1
LWC	±50%	−0.1/0.2	NS/NS	0.1/0.3
IWC	±70%	−2.3/5.0	NS/NS	0.4/−0.9
Liquid $R_{\text{eff}}$	±25%	0.6/−0.6	NS/NS	−0.2/0.2
Ice $R_{\text{eff}}$	±25%	1.2/−1.5	NS/NS	−0.1/0.2
<i>CALIPSO</i> or MODIS properties				
<i>CALIPSO</i> OD	±50%	−0.3/0.1	NS/NS	NS/NS
<i>CALIPSO</i> IWC	2×/÷2	−0.8/0.4	NS/NS	0.1/NS
<i>CALIPSO</i> LWC	±20%	−0.1/0.1	NS/NS	0.5/−0.7
Liquid $R_{\text{eff}}$	±3 $\mu\text{m}$	NS/−0.5	NS/NS	−0.2/0.5
Ice $R_{\text{eff}}$	±10 $\mu\text{m}$	0.2/−0.7	NS/NS	NS/NS
MODIS OD	±20%	−0.1/NS	NS/NS	NS/NS
All clouds				
Base height	±240 m	0.4/−0.4	NS/NS	−1.5/1.6
Top height	±240 m	−1.1/1.0	NS/NS	0.6/−0.5
<i>CALIPSO</i> aerosol properties				
AOD	2×/÷2	−0.3/0.2	NS/NS	0.6/−0.4
Smoke = dust	—	NS	NS	−0.1
All dust	—	NS	NS	−0.3
All smoke	—	−0.1	NS	NS
Environmental properties				
Temperature	±2 K above 500 hPa	2.7/−2.8	NS/NS	0.1/−0.1
Temperature	±2 K below 500 hPa	3.3/−3.4	NS/NS	3.8/−3.8
Specific humidity	±25% above 500 hPa	−1.7/1.8	NS/NS	NS/NS
Specific humidity	±25% below 500 hPa	−2.0/2.1	NS/NS	8.3/−10.1
Surface temperature	±2 K	1.1/−1.1	11.2/−11.0	5.5/−5.4
Surface albedo	Increase ±10%	NS/NS	NS/NS	NS/NS

profile, and then the effect on the corresponding global fluxes in either the LW or SW. Perturbations are rooted directly in corresponding uncertainty analyses from the component datasets. Microphysical perturbations for *CloudSat* are derived from error propagation included in the 2B-CWC-RO and 2C-PRECIP-COLUMN products (Austin et al. 2009; Haynes et al. 2009), and MODIS uncertainties are documented by Nakajima and King (1990). Perturbations in ECMWF parameters are pulled from comparisons with radiosondes (Divakarla et al. 2006). *CALIPSO* aerosol uncertainties mentioned above are also included in the tables. As stated in the previous section, errors can vary with different spatial and temporal scales. When using global datasets, it is important to recognize the scale of the region and time period to minimize error.

The largest uncertainties in LW flux estimates derive from errors in surface temperatures and changes in specific humidity below the 500-hPa level. Whereas the effect is smaller at the TOA, the emission by the surface changes  $\pm 11 \text{ W m}^{-2}$  for an alteration of  $\pm 2 \text{ K}$ , yielding an approximate error estimate of the impact of extrapolating daily LW flux estimates from the limited twice-daily

sampling of the A-Train sensors. This, in turn, leads to uncertainties in the emission from the atmosphere back to the surface of  $5.5 \text{ W m}^{-2}$ . The LW fluxes are also vulnerable to error in atmospheric temperature and specific humidity profiles. Changes in temperature and water vapor in the lower troposphere impact OLR by up to  $3.4 \text{ W m}^{-2}$ . Systematic changes in temperature and water vapor in the lower troposphere, however, have an intensified effect at the surface because of the larger concentrations of water vapor at lower levels, leading to uncertainties up to  $10.1 \text{ W m}^{-2}$  in SLR. Additional uncertainties in LW surface fluxes arise from errors in cloud height, which can only be determined to approximately  $\pm 240 \text{ m}$  with *CloudSat*. Increasing or decreasing cloud-base height by 240 m causes differences in surface radiation of  $1.5 \text{ W m}^{-2}$ . Similar effects are found for altering cloud-top heights, but to a slightly lesser degree.

Uncertainties in SW fluxes are dominated by cloud microphysical properties. Perturbing LWC alters the reflection and absorption properties of clouds, resulting in uncertainties of 5.5 and  $-3.1 \text{ W m}^{-2}$  in SSR for downward and upward perturbations, respectively.

TABLE 7. As in Table 6, but for SW fluxes.

Parameter	Perturbation	$\Delta F_{SW,TOA}^{\uparrow}$	$\Delta F_{SW,SFC}^{\uparrow}$	$\Delta F_{SW,SFC}^{\downarrow}$
<i>CloudSat</i> -only properties				
Precipitation	2×/none	0.2/−0.4	NS/NS	−0.3/0.4
LWC	±50%	2.7/−4.9	−0.3/−0.5	−3.1/5.5
IWC	±70%	2.2/−3.2	−0.2/0.3	−2.4/3.7
Liquid $R_{eff}$	±25%	−2.5/2.8	−0.2/0.2	2.5/−2.8
Ice $R_{eff}$	±25%	−1.1/1.5	NS/NS	0.9/−1.3
<i>CALIPSO</i> or MODIS properties				
<i>CALIPSO</i> OD	±50%	NS/NS	NS/NS	NS/NS
<i>CALIPSO</i> IWC	2×/÷2	NS/NS	NS/NS	−0.1/NS
<i>CALIPSO</i> LWC	±20%	0.6/−0.7	NS/NS	−0.8/0.8
Liquid $R_{eff}$	±3 $\mu\text{m}$	−1.2/1.2	0.1/−0.1	1.5/−1.4
Ice $R_{eff}$	±10 $\mu\text{m}$	NS/NS	NS/NS	NS/−0.1
MODIS OD	±20%	NS/NS	NS/NS	NS/NS
All clouds				
Base height	±240 m	−2.7/3.2	0.3/−0.3	3.2/−3.9
Top height	±240 m	3.1/−2.3	−0.3/0.2	−3.5/2.4
<i>CALIPSO</i> aerosol properties				
AOD	2×/÷2	0.8/−0.4	0.3/−0.4	−2.9/1.6
Smoke = dust	—	0.2	NS	0.6
All dust	—	0.5	NS	0.7
All smoke	—	−0.6	−0.2	−1.7
Environmental properties				
Temperature	±2 K above 500 hPa	NS/NS	NS/NS	NS/NS
Temperature	±2 K below 500 hPa	0.1/−0.1	NS/NS	−0.2/0.2
Specific humidity	±25% above 500 hPa	−0.1/0.1	NS/NS	−0.1/NS
Specific humidity	±25% below 500 hPa	−0.5/0.6	−0.2/0.2	−2.2/2.6
Surface temperature	±2 K	NS/NS	NS/NS	NS/NS
Surface albedo	Increase ±10%	1.4/−1.4	1.8/−1.8	0.3/−0.3

Effects of similar magnitudes are observed at the TOA. Shortwave fluxes are also sensitive to the increase/decrease of low cloud height because of the implied change in liquid water path. Similar effects occur when effective radii are perturbed. Systematic changes in the *CloudSat* liquid effective radii are most significant, resulting in errors of about  $2.8 \text{ W m}^{-2}$  at the TOA and the surface. Environmental perturbations are most noticeable in the lower troposphere where water vapor is more prevalent. Perturbing lower-tropospheric specific humidity reveals uncertainties from  $-2.2$  to  $2.6 \text{ W m}^{-2}$ . Errors in surface albedo in the six SW bands between  $0.65$  and  $3.74 \mu\text{m}$  are estimated by perturbing the value for each surface in the radiative transfer model by 10%, leading to errors of about  $1.4$  and  $1.8 \text{ W m}^{-2}$  in the reflected fluxes at the TOA and the surface, respectively.

Uncertainties in *CALIPSO* cloud detection reveal errors of smaller magnitude, mostly resulting from the smaller sample size of undetected clouds globally. Of the samples in a *CloudSat* granule, on average 8% contain a cirrus cloud detected only by *CALIPSO* and 16% contain an undetected low-level cloud, one-third of which have properties that are based on MODIS data.

Therefore it is logical that errors in the representation of undetected low-level clouds have the highest global impact in SW of  $\sim 1.5 \text{ W m}^{-2}$  at the TOA and the surface.

## 7. Summary

Earth's radiative budget has been a topic of study for many years, but it was not until the launch of *CloudSat* and *CALIPSO* that observational constraints on the vertical distributions of cloud and aerosol properties have been available on global scales. The combination of the *CloudSat* CPR, CALIOP on *CALIPSO*, and MODIS on *Aqua* provides a more comprehensive dataset of cloud and aerosol locations and properties. By including observations from all three of these sensors, the 2B-FLXHR-LIDAR dataset benefits from a more complete description of cloud and aerosol occurrence and properties than does the radar-only 2B-FLXHR product, enabling more accurate modeling of radiation within the atmosphere. The 2C-PRECIP-COLUMN product provides a more robust representation of precipitation, MODIS optical depths and cloud properties provide more detail for undetected low clouds, and *CALIPSO*

backscatter improves optical-depth information for undetected cirrus and aerosol. These new data will help to advance our understanding of the impacts of clouds and aerosol on radiative budget not only at atmospheric boundaries but throughout the atmosphere.

Uncertainties in the 2B-FLXHR-LIDAR flux estimates were determined through a combination of comparisons with CERES and sensitivity studies. RMS differences between estimated TOA fluxes and collocated CERES observations reveal that uncertainties in monthly/ $5^\circ$  average OSR and OLR are  $16.5$  and  $5.7 \text{ W m}^{-2}$ , respectively, and that biases are  $4.1$  and  $-4.9 \text{ W m}^{-2}$ . RMS differences decrease with increasing spatial and time scales. Sensitivity studies suggest that errors in SW fluxes are dominated by *CloudSat* LWC estimates and, to a lesser extent, the assumed properties of undetected low clouds. Errors in LW fluxes are dominated by uncertainty in prescribed skin temperature and lower-tropospheric water vapor.

Using the more complete picture provided by these multisensor A-Train datasets, the impacts of clouds and aerosols on radiative fluxes at the top of the atmosphere and at the surface are documented based on more than 4 yr of observations. On a global basis, clouds are found to exert a net cooling of approximately  $-18.1 \pm 3.7 \text{ W m}^{-2}$  at the TOA and  $-26.7 \text{ W m}^{-2}$  at the surface in the 2B-FLXHR-LIDAR dataset. The benefits of adopting a multisensor approach are emphasized by the fact that low clouds undetected by *CloudSat* increase outgoing SW radiation by  $8.4 \text{ W m}^{-2}$  and decrease the SW flux at the surface by  $9.3 \text{ W m}^{-2}$ , globally. Undetected low clouds also increase LW emission back to the surface by  $8.1 \text{ W m}^{-2}$ . Undetected cirrus have little impact on SW fluxes but are effective in trapping LW radiation, resulting in a decrease in OLR of  $1.1 \text{ W m}^{-2}$ . Aerosols were found to exert a cooling of  $-2.5 \pm 0.8 \text{ W m}^{-2}$  in clear skies over ocean and  $-1.6 \pm 0.5 \text{ W m}^{-2}$  in all-sky conditions globally—less than in previous studies that were based on passive observations but more consistent with the range of estimates from previous modeling studies. These results provide benchmarks against which the ability of models to represent cloud radiative effects on seasonal time scales can be assessed, especially if the models are sampled to coincide with the 0130/1330 local time overpass times of *CloudSat*.

The 2B-FLXHR-LIDAR algorithm is an operational algorithm and will be continually improved in the future as more advanced data products are developed and evaluated. Improved estimates of the microphysical properties of thin cirrus clouds and identification of mixed-phase clouds from a combination of *CALIPSO* and *CloudSat* observations, for example, have recently

become available and offer the potential to limit assumptions and realize improvements in future versions of the algorithm.

*Acknowledgments.* This research was supported by NASA *CloudSat* Mission Grants NAS5-99237 and NASA JPL 1439268. The authors thank the staff at the *CloudSat* Data Processing Center (DPC) for their help in data processing. The authors also thank Norm Wood and Colette Heald for assisting with *CALIPSO* data. All *CloudSat* data presented here were acquired through the DPC and at the time of writing could be accessed online (<http://www.cloudsat.cira.colostate.edu>). *CALIPSO* data were obtained online from the ASDC (<http://eosweb.larc.nasa.gov>).

#### REFERENCES

- Austin, R. T., 2007: Level 2b Radar-Only Cloud Water Content (2B-CWC-RO) process description document. *CloudSat* Data Processing Center, 24 pp. [Available online at <http://cloudsat.cira.colostate.edu/data/CDlist.php?go=list&path=/2B-CWC-RO>.]
- , A. J. Heymsfield, and G. L. Stephens, 2009: Retrieval of ice cloud microphysical parameters using the *CloudSat* millimeter-wave radar and temperature. *J. Geophys. Res.*, **114**, D00A23, doi:10.1029/2008JD010049.
- Barkstrom, B. R., 1984: The Earth Radiation Budget Experiment (ERBE). *Bull. Amer. Meteor. Soc.*, **65**, 1170–1185.
- Berg, W., T. L'Ecuyer, and J. M. Haynes, 2010: The distribution of rainfall over oceans from spaceborne radars. *J. Appl. Meteor. Climatol.*, **49**, 535–543.
- Chand, D., R. Wood, T. Anderson, S. Satheesh, and R. Charlson, 2009: Satellite-derived direct radiative effect of aerosols dependent on cloud cover. *Nat. Geosci.*, **2**, 181–184.
- Comstock, J. M., and K. Sassen, 2001: Retrieval of cirrus cloud radiative and backscattering properties using combined lidar and infrared radiometer (LIRAD) measurements. *J. Atmos. Oceanic Technol.*, **18**, 1658–1673.
- D'Almeida, G. A., P. Koepke, and E. P. Shettle, 1991: *Atmospheric Aerosols: Global Climatology and Radiative Characteristics*. A. Deepak, 561 pp.
- Deepak, A., and H. E. Gerber, Eds., 1983: Report of the Experts Meeting on Aerosols and their Climatic Effects. World Climate Program Series, Vol. 55, World Meteorological Organization, 107 pp.
- Divakarla, M., G. C. D. Barnet, M. D. Goldberg, L. M. McMillin, E. Maddy, L. Z. W. Wolf, and X. Liu, 2006: Validation of atmospheric infrared sounder temperature and water vapor retrievals with matched radiosonde measurements and forecasts. *J. Geophys. Res.*, **111**, D09S15, doi:10.1029/2005JD006116.
- Ellis, J. S., and T. H. VonderHaar, 1976: Zonal average radiation budget measurements from satellites for climate studies. Dept. of Atmospheric Sciences, Colorado State University, Atmospheric Science Paper 240, 57 pp.
- Fu, Q., and K. N. Liou, 1992: On the correlated *k*-distribution method for radiative transfer in nonhomogeneous atmospheres. *J. Atmos. Sci.*, **49**, 2139–2156.
- Haladay, T., and G. Stephens, 2009: Characteristics of tropical thin cirrus clouds deduced from joint *CloudSat* and *CALIPSO*

- observations. *J. Geophys. Res.*, **114**, D00A25, doi:10.1029/2008JD010675.
- Harrison, E. F., P. Minnis, B. R. Barkstrom, V. Ramanathan, R. D. Cess, and G. G. Gibson, 1990: Seasonal variation of cloud radiative forcing derived from the Earth Radiation Budget Experiment. *J. Geophys. Res.*, **95**, 18 687–18 703.
- Hartmann, D. L., V. Ramanathan, A. Berroir, and G. E. Hunt, 1986: Earth radiation budget data and climate research. *Rev. Geophys.*, **24**, 439–468.
- Haynes, J. M., T. S. L'Ecuyer, G. L. Stephens, C. M. S. D. Miller, N. B. Wood, and S. Tanelli, 2009: Rainfall retrieval over the ocean with spaceborne W-band radar. *J. Geophys. Res.*, **114**, D00A22, doi:10.1029/2008JD009973.
- Holz, R., S. Ackerman, F. Nagle, R. Frey, S. Dutcher, R. K. M. Vaughan, and B. Baum, 2008: Global Moderate Resolution Imaging Spectroradiometer (MODIS) cloud detection and height evaluation using CALIOP. *J. Geophys. Res.*, **113**, D00A19, doi:10.1029/2008JD009837.
- Kato, S., and Coauthors, 2011: Improvements of top-of-atmosphere and surface irradiance computations with CALIPSO-, CloudSat-, and MODIS-derived cloud and aerosol properties. *J. Geophys. Res.*, **116**, D19209, doi:10.1029/2011JD016050.
- Kaufman, Y. J., and Coauthors, 2005: A critical examination of the residual cloud contamination and diurnal sampling effects on MODIS estimates of aerosol over ocean. *IEEE Trans. Geosci. Remote Sens.*, **43**, 2886–2897.
- Kiehl, J. T., and K. E. Trenberth, 1997: Earth's annual global energy budget. *Bull. Amer. Meteor. Soc.*, **78**, 197–208.
- Kittaka, C., D. M. Winker, M. A. Vaughan, A. Omar, and L. A. Remer, 2005: Top-of-atmosphere direct radiative effect of aerosols over global oceans from merged CERES and MODIS observations. *J. Climate*, **18**, 3506–3526.
- , —, —, —, and —, 2011: Intercomparison of column aerosol optical depths from CALIPSO and MODIS-Aqua. *Atmos. Meas. Tech.*, **4**, 131–141.
- Lebsack, M. D., and T. S. L'Ecuyer, 2011: The retrieval of warm rain from CloudSat. *J. Geophys. Res.*, **116**, D20209, doi:10.1029/2011JD016076.
- , —, and G. L. Stephens, 2011: Detecting the ratio of rain and cloud water in low-latitude shallow marine clouds. *J. Appl. Meteor. Climatol.*, **50**, 419–432.
- L'Ecuyer, T., N. Wood, T. Haladay, G. L. Stephens, and P. W. Stackhouse, 2008: Impact of clouds on atmospheric heating based on the R04 CloudSat fluxes and heating rates data set. *J. Geophys. Res.*, **113**, D00A15, doi:10.1029/2008JD009951.
- Lo, C., J. M. Comstock, and C. Flynn, 2006: An Atmospheric Radiation Measurement value-added product to retrieve optically thin cloud visible optical depth using micropulse lidar. U.S. Dept. of Energy Rep. DOE/SC-ARM/TR-077, 11 pp. [Available online at [http://www.arm.gov/publications/tech\\_reports/doe-sc-arm-tr-077.pdf](http://www.arm.gov/publications/tech_reports/doe-sc-arm-tr-077.pdf).]
- Loeb, N. G., and S. Kato, 2002: Top-of-atmosphere direct radiative effect of aerosols over the tropical oceans from the Clouds and the Earths Radiant Energy System (CERES) satellite instrument. *J. Climate*, **15**, 1474–1484.
- Mace, G. G., Q. Zhang, M. Vaughan, R. Marchand, G. Stephens, C. Trepte, and D. Winker, 2009: A description of hydrometeor layer occurrence statistics derived from the first year of merged CloudSat and CALIPSO data. *J. Geophys. Res.*, **114**, D00A26, doi:10.1029/2007JD009755.
- Menzel, W., and Coauthors, 2008: MODIS global cloud-top pressure and amount estimation: Algorithm description and results. *J. Appl. Meteor. Climatol.*, **47**, 1175–1198.
- Miles, N. L., J. Verlinde, and E. E. Clothiaux, 2000: Cloud droplet size distributions in low-level stratiform clouds. *J. Atmos. Sci.*, **57**, 295–311.
- Mitchell, D. L., A. Macke, and Y. Liu, 1996: Modeling cirrus clouds. Part II: Treatment of radiative properties. *J. Atmos. Sci.*, **53**, 2967–2988.
- Nakajima, T., and M. D. King, 1990: Determination of the optical thickness and effective particle radius of clouds from reflected solar radiation measurements. Part I: Theory. *J. Atmos. Sci.*, **47**, 1878–1893.
- Naud, C., J.-P. Muller, E. E. Clothiaux, B. A. Baum, and W. P. Menzel, 2005: Intercomparison of multiple years of MODIS, MISR and radar cloud-top heights. *Ann. Geophys.*, **23**, 2415–2424.
- Omar, A., and Coauthors, 2009: The CALIPSO automated aerosol classification and lidar ratio selection algorithm. *J. Atmos. Oceanic Technol.*, **26**, 1994–2014.
- Ramanathan, V., R. D. Cess, E. F. Harrison, P. Minnis, B. R. Barkstrom, E. Ahmad, and D. Hartmann, 1989: Cloud-radiative forcing and climate: Results from the Earth Radiation Budget Experiment. *Science*, **243**, 57–63.
- Raschke, E., A. Ohmura, W. B. Rossow, B. E. Carlson, Y.-C. Zhang, C. Stubenrauch, M. Kottek, and M. Wild, 2005: Cloud effects on the radiation budget based on ISCCP data (1991 to 1995). *Int. J. Climatol.*, **25**, 1103–1125.
- Remer, L. A., and Y. J. Kaufman, 2006: Aerosol direct radiative effect at the top of the atmosphere over cloud free ocean derived from four years of MODIS data. *Atmos. Chem. Phys.*, **6**, 237–253.
- Ritter, B., and J.-F. Geleyn, 1992: A comprehensive radiation scheme for numerical weather prediction models with potential applications in climate simulations. *Mon. Wea. Rev.*, **120**, 303–324.
- Rossow, W. B., and Y.-C. Zhang, 1995: Calculation of surface and top of atmosphere radiative fluxes from physical quantities based on ISCCP data sets. 2: Validation and first results. *J. Geophys. Res.*, **100**, 1167–1197.
- Sassen, K., Z. Wang, and D. Liu, 2009: Cirrus clouds and deep convection in the tropics: Insights from CALIPSO and CloudSat. *J. Geophys. Res.*, **114**, D00H06, doi:10.1029/2009JD011916.
- Schiffer, R. A., and W. B. Rossow, 1983: The International Satellite Cloud Climatology Project (ISCCP): The first project of the World Climate Research Programme. *Bull. Amer. Meteor. Soc.*, **64**, 779–784.
- Stackhouse, P. W., D. P. Kratz, G. R. McGarragh, S. K. Gupta, and E. B. Greer, 2006: Fast longwave and shortwave flux (FLASHflux) products from CERES and MODIS measurements. Preprints, *12th Conf. on Atmospheric Radiation*, Madison, WI, Amer. Meteor. Soc., P1.10. [Available online at <http://ams.confex.com/ams/pdfpapers/113479.pdf>.]
- Stephens, G. L., 1978: Radiation profiles in extended water clouds. II: Parameterization schemes. *J. Atmos. Sci.*, **35**, 2123–2132.
- , 1980: Radiative properties of cirrus clouds in the infrared region. *J. Atmos. Sci.*, **37**, 435–446.
- , 2005: Cloud feedbacks in the climate system: A critical review. *J. Climate*, **18**, 237–273.
- , G. G. Campbell, and T. H. VonderHaar, 1981: Earth radiation budgets. *J. Geophys. Res.*, **86**, 9739–9760.
- , P. W. Stackhouse Jr., and F. J. Flatau, 1990: The relevance of the microphysical and radiative properties of cirrus clouds to climate and climate feedback. *J. Atmos. Sci.*, **47**, 1742–1753.

- , and Coauthors, 2002: The *CloudSat* Mission and the A-Train: A new dimension to space-based observations of clouds and precipitation. *Bull. Amer. Meteor. Soc.*, **83**, 1771–1790.
- , and Coauthors, 2010: The dreary state of precipitation in global models. *J. Geophys. Res.*, **115**, D24211, doi:10.1029/2010JD014532.
- , M. Wild, P. W. Stackhouse, T. L'Ecuyer, S. Kato, and D. S. Henderson, 2012: The global character of the flux of downward longwave radiation. *J. Climate*, **25**, 2329–2340.
- Takemura, T., T. Nakajima, O. Dubovik, B. N. Holben, and S. Kinne, 2002: Single-scattering albedo and radiative forcing of various aerosol species with a global three-dimensional model. *J. Climate*, **15**, 333–352.
- Trenberth, K. E., J. T. Fasullo, and J. Kiehl, 2009: Earth's global energy budget. *Bull. Amer. Meteor. Soc.*, **90**, 311–323.
- Trepte, Q. Z., P. Minnis, C. R. Trepte, S. Sun-Mack, and R. Brown, 2010: Improved cloud detection in CERES Edition 3 algorithm and comparison with the *CALIPSO* Vertical Feature Mask. *Proc. 13th Conf. on Atmospheric Radiation and Cloud Physics*, Portland, OR, Amer. Meteor. Soc., JP1.32. [Available online at <https://ams.confex.com/ams/13CldPhy13AtRad/webprogram/Paper171785.html>.]
- VonderHaar, T. H., and V. E. Suomi, 1971: Measurements of the earth's radiation budget from satellites during a five-year period. Part I: Extended time and space means. *J. Atmos. Sci.*, **28**, 305–314.
- Wielicki, B. A., B. R. Barkstrom, E. F. Harrison, R. B. Lee III, G. L. Smith, and J. E. Cooper, 1996: Clouds and the Earth's Radiant Energy System (CERES): An Earth Observing System experiment. *Bull. Amer. Meteor. Soc.*, **77**, 853–868.
- Winker, D. M., W. H. Hunt, and C. A. Hostetler, 2004: Status and performance of the CALIOP lidar: Laser radar techniques for atmospheric sensing. *Laser Radar Techniques for Atmospheric Sensing*, U. N. Singh, Ed., International Society for Optical Engineering (SPIE Proceedings, Vol. 5575), 8–15.
- , —, and M. J. McGill, 2007: Initial performance assessment of CALIOP. *Geophys. Res. Lett.*, **34**, L19803, doi:10.1029/2007GL030135.
- Yu, H., and Coauthors, 2006: A review of measurement-based assessment of aerosol direct radiative effect and forcing. *Atmos. Chem. Phys.*, **6**, 613–666.
- Zhang, J., S. A. Christopher, L. A. Remer, and Y. J. Kaufmann, 2005: Shortwave aerosol radiative forcing over cloud-free oceans from *Terra*: 2. Seasonal and global distributions. *J. Geophys. Res.*, **110**, D10S24, doi:10.1029/2004JD005009.